Hexcomb Pattern Roughness Effects on Blunt Body Transition and Heating

Brian R. Hollis*
NASA Langley Research Center, Hampton, VA 23681

An experimental investigation of hexcomb pattern surface roughness effects on boundary-layer transition and convective heating has been performed. Two representative entry vehicle geometries, a spherical-cap aeroshell and a sphere-cone aeroshell, were considered. Multiple cast ceramic models of each geometry were fabricated with various roughness pattern densities and depths that simulated an ablated hexcomb-structure thermal protection system. Wind tunnel testing was performed at Mach 6 over a range of Reynolds numbers sufficient to produce laminar, transitional, and turbulent flow. Aeroheating and boundary-layer transition onset data were obtained using global phosphor thermography. The experimental heating data are presented herein, as are comparisons to laminar and turbulent smooth-wall heat transfer distributions from computational flow field simulations. The experimental data were used to develop a unified boundary-layer transition correlation for both sandgrain distributed roughness and hexcomb pattern roughness.

I. Nomenclature

d	hexcomb width (m) or (in.) or (mil)
h	hexcomb depth (m) or (in.)
h	heat transfer film coefficient (kg/m^2.s)
h_{FR}	Fay-Riddell value of heat transfer film coefficient (kg/m^2.s)
H_0	total enthalpy (J/kg)
H_{AW}	adiabatic wall enthalpy (J/kg)
H_e	boundary layer edge enthalpy (J/kg)
H_k	roughness height enthalpy (J/kg)
H_w	wall enthalpy (J/kg)
M_e	boundary layer edge Mach number
M_∞	free stream Mach number
r_{stag}	radius of stagnation region M_e boundary
R	model base radius (m) or (in)
R_C	model corner radius (m) or (in)
R_N	model nose radius (m) or (in)
Re_θ	momentum thickness Reynolds number
$Re_{\theta,TR}$	momentum thickness Reynolds number at transition
Re_∞	unit free stream Reynolds number (1/m) or (1/ft)
s	streamline distance from stagnation region M_e boundary
s_0	streamline distance from stagnation point
T_e	boundary layer edge temperature (K)
T_w	wall temperature (K)
U_e	boundary layer edge total velocity (m/s)
U_∞	free stream velocity (m/s)
(x,y,z)	Cartesian coordinates (m)
X_{TR}	transition correlation disturbance parameter
Y_{TR}	transition correlation flow field parameter

* Aerothermodynamics Branch Senior Technical Lead, AIAA Associate Fellow

β_N model nose included angle (deg.)
β_{POHL} modified Pohlhausen parameter
δ boundary-layer height (m)
ϕ streamline terminus angular position (deg.)
λ_{POHL} Pohlhausen parameter
ρ_e boundary-layer edge density (kg/m^3)
ρ_∞ free stream density (kg/m^3)
ν_e boundary-layer edge kinematic viscosity (m^2/s)
θ boundary-layer momentum thickness (m)

II. Background and Introduction

In this work, the effects of hexcomb pattern surface roughness on boundary-layer transition and heating augmentation are considered. Roughness data were obtained through hypersonic wind tunnel testing of a set of representative entry vehicle geometries with roughness patterns that simulated those produced by the ablation of a hexcomb-structure thermal protection system (TPS). Representative data from this study will be shown herein and the complete data set is presented in detail in Ref. 1.

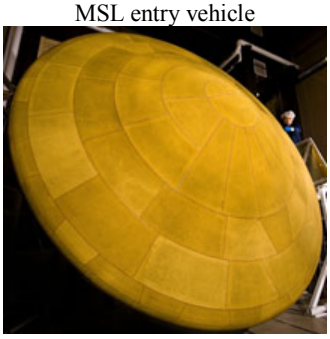
"Roughness" is a generic term in aerospace literature that encompasses many types of surface features that deviate from that of a smooth outer mold line (OML). Roughness can be divided into two general types: discrete and distributed. Discrete roughness (Figure 1) includes surface features such as: a) protruding compression pads or recessed cavities at mechanical attachment points; b) steps or gaps between heat shield tiles resulting from differential ablation of the tiles and the filler material between them; and c) physical damage to a TPS. Distributed roughness (Figure 2) includes features such as: a) regular patterns such as those resulting from ablation of hexcomb-structure TPS; b) irregular deflections of a flexible TPS under aerodynamic loading; c) random "sandgrain" features resulting from ablation of a monolithic TPS; or d) the texture of overlapping fibers on a woven TPS.

Heat shield attachment point cavity on Genesis entry vehicle



a) Cavities and protrusions

Block panel layout of TPS on MSL entry vehicle



b) Block TPS steps and gaps

Damaged TPS tiles on Shuttle Orbiter



c) Physical damage to TPS

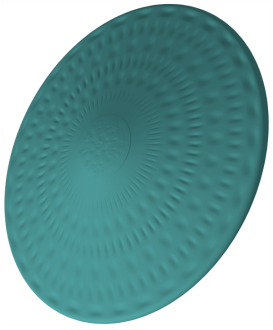
Figure 1. Discrete surface roughness types.

Hexcomb cavities on Apollo ablated TPS



a) Pattern TPS ablation

Flexible TPS deflections over supporting structures



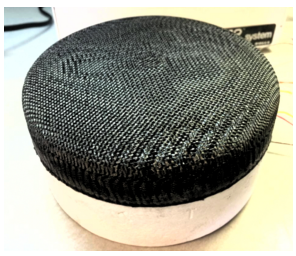
b) Flexible TPS deflections

Ablation of monolithic TPS on Stardust capsule



c) Sand grain TPS ablation

Arc jet test coupon of woven TPS material



c) Woven TPS

Figure 2. Distributed surface roughness types.

Data on the effects of surface roughness are valuable because the roughness of an entry vehicle's TPS can promote earlier boundary-layer transition and produce higher turbulent heating (and shear) levels than would be expected based on an idealized, smooth-wall analysis. However, due to the complexities of roughness effects, a vehicle's TPS is typically designed using analytical, computational, and/or experimental techniques that are based on the assumption of a smooth surface. The effects of roughness on the aerothermodynamic environment can then be included through approximate engineering correlations and methods.

The purpose of this test program was to obtain data on the effects of distributed hexcomb pattern type roughness. These data are intended for use in the development and/or validation of engineering correlations for the effects of hexcomb pattern roughness on boundary-layer transition and turbulent heat transfer. They can also serve as the basis for development and/or validation of higher-fidelity, numerical flow-field simulation models for roughness effects.

Examples of ablating TPS that produce such patterns include the Avcoat material used on the Apollo capsules and the Orion EFT-1 flight test vehicle and the SLA-561V material used on the Mars Viking, Mars Exploration Rover, and Mars Pathfinder entry vehicles. These growth of hexcomb ablation patterns can be seen by comparing the pretest (Figure 3a) and post-test (Figure 3b) photographs of an Avcoat sample coupon subjected to an arc jet flow for material response testing.



a) Pretest **b) Post test**

Figure 3. Arc jet test sample coupon of Avcoat hexcomb TPS (from [2]).

III. Experimental and Computational Methods

A. Wind Tunnel Models

Roughness effects data were obtained on two representative entry vehicle geometries: a spherical-cap geometry (Figure 4) and a sphere-cone geometry (Figure 5). The spherical-cap geometry is similar to that of the Mercury – Gemini – Apollo – Orion family of entry vehicles employed in NASA's crewed space program. The sphere-cone geometry is similar to that of the Mars Viking – Mars Pathfinder – Mars Exploration Rover – Mars Phoenix – Mars Science Laboratory – Mars 2020 family of entry vehicle used in NASA's robotic Mars exploration program. Geometric parameters for both configurations are listed in Table 1. Multiple models of each configuration were fabricated through ceramic casting with a range of hexcomb roughness patterns as detailed in Ref. 1.

The parametric range of hexcomb densities and depths is detailed in Table 2. There were two limitations on fabrication capabilities that defined the range of pattern parameters. The first was the minimum resolution of the stereolithographic apparatus (SLA) used to make model patterns. The SLA resolution was on the order of 0.001 in. and thus, the minimum hexcomb depth considered was 0.0015 inches. The second limitation was the memory of the computer used to generate the CAD files for the SLA system, which allowed a maximum of 3700 hexcombs per model. A total of 7 patterns were generated for each geometry with hexcomb depths of 0.0015 in. to 0.0100 in. and either 1200 or 3700 hexcombs. The nomenclature for identifying the model and hexcomb pattern was *Geometry - number of hexcombs - hexcomb depth*; e.g., *Spherical-cap 3700-0100*, which identifies the spherical-cap geometry model with 3700 hexcombs of 0.0100 in. depth.

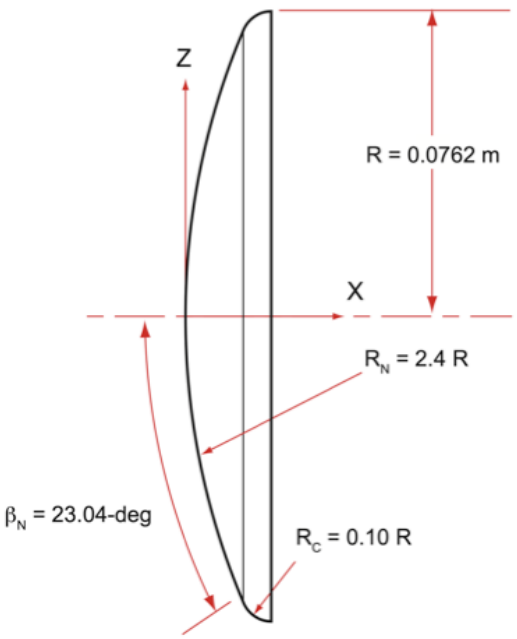


Figure 4. Spherical-cap model geometry.

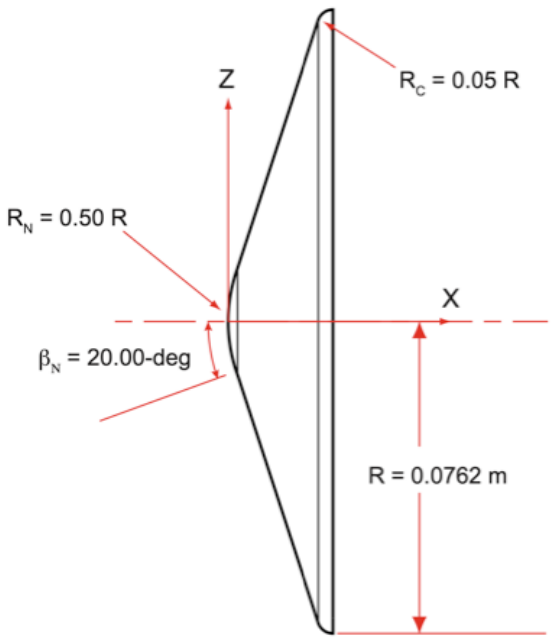


Figure 5. Sphere-cone model geometry.

Table 1. Wind tunnel model geometry parameters.

Model Geometry	Model radius, R		Nose radius, R_N		Shoulder radius, R_C		Nose angle, β_N	R_N/R	R_C/R
	in.	m	in.	m	in.	m	deg.		
Spherical-cap	3.000	0.0762	7.200	0.1829	0.3000	0.00762	23.04	2.4	0.100
Sphere-cone	3.000	0.0762	1.500	0.0371	0.1500	0.00381	20.00	0.5	0.050

Table 2. Wind tunnel model hexcomb parameters.

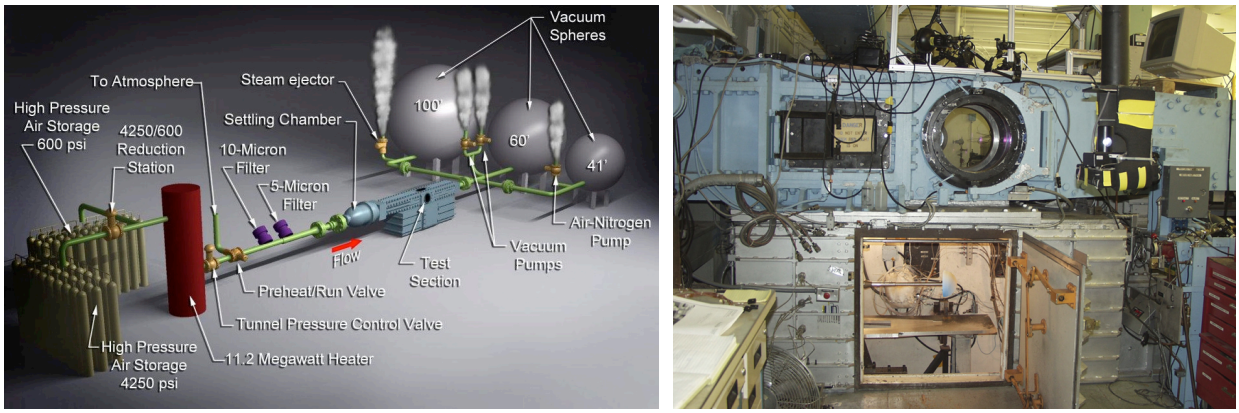
Hexcomb Pattern	Number of hexcombs	Hexcomb depth, h			Hexcomb width, d		d/h
		in.	mil	m	in.	m	
Smooth	N/A	N/A	N/A	N/A	N/A	N/A	N/A
1200-0025	1200	0.0025	2.5	6.350E-05	0.1300	3.302E-03	52.0
1200-0025	1200	0.0050	5.0	1.270E-04	0.1300	3.302E-03	26.0
1200-0050	1200	0.0100	10.0	2.540E-04	0.1300	3.302E-03	13.0
3700-0015	3700	0.0015	1.5	3.810E-05	0.0650	1.651E-03	43.3
3700-0025	3700	0.0025	2.5	6.350E-05	0.0650	1.651E-03	26.0
3700-0050	3700	0.0050	5.0	1.270E-04	0.0650	1.651E-03	13.0
3700-0100	3700	0.0100	10.0	2.540E-04	0.0650	1.651E-03	6.5

B. Wind Tunnel Test Facility and Operating Conditions

1. Facility Description

Wind tunnel testing was performed in the 20-Inch Mach 6 Air Tunnel of the NASA Langley Aerothermodynamics Laboratory (LAL). The 20-Inch Mach 6 Air Tunnel (Figure 6) is a blow-down to atmosphere facility in which heated, dried, and filtered air is used as the test gas. The tunnel has a two-dimensional contoured nozzle that opens into a 20.5 in. × 20.0 in. test section. The tunnel is equipped with a bottom-mounted injection system with a -5 deg. to +55 deg.

pitch range and ±5 deg. yaw range that can transfer a model from a sheltered model box to the tunnel centerline in less than 0.5 sec. Run times of up to 15 minutes are possible in this facility, although for aeroheating studies, run times of only a few seconds are typically required. The nominal reservoir conditions of this facility produce perfect-gas free stream flows with Mach numbers between 5.8 and 6.1 and unit Reynolds numbers of 0.5×10^6/ft to 8.3×10^6/ft. With its wide Reynolds number operating range capable of producing laminar, transitional, or turbulent flow on most geometries, this tunnel is primarily used for heat-transfer and boundary-layer transition studies. More detailed information on this and other LAL facilities can be found in Refs. 3-4.



a) Schematic **b) Test section**

Figure 6. Langley Research Center 20-Inch Mach 6 Air Tunnel.

2. Facility Operating Conditions

Data were obtained during Test 6991 in the 20-Inch Mach 6 Air Tunnel at six unit Reynolds numbers from $Re_\infty = 3.0\times10^6$/ft to 8.3×10^6/ft. These conditions are listed in Table 3. All spherical-cap data were obtained at $\alpha = 28$ deg. and all sphere-cone data were obtained at $\alpha = 16$ deg. The angles of attack were chosen for continuity with smooth-OML data obtained in prior testing of the Orion entry vehicle and the Mars Science Laboratory entry vehicle (e.g., Ref. 5).

Free stream values for velocity (U_∞), density (ρ_∞), temperature (T_∞), unit Reynolds number (Re_∞), and Mach number (M_∞) for the run conditions are listed in Table 3. Additionally, the enthalpy difference (ΔH_{tot}), and reference heat transfer film-coefficient value (h_{FR}) are provided. The enthalpy term is defined as the difference $H_0 - H_{300K}$ between the free stream total enthalpy and the wall enthalpy at cold wall (300 K) conditions. The film coefficient is the value from the Fay-Riddell theory (Ref. 5) for a hemispherical radius at cold wall (300 K) conditions, where the radius is the nose radius of the model geometry.

Table 3. Run conditions for Test 6991, 20-Inch Mach 6 Air Tunnel.

Re_∞ (1/ft)	Re_∞ (1/m)	M_∞	T_∞ (K)	ρ_∞ (kg/m^3)	U_∞ (m/s)	ΔH_{tot} (MJ/kg)	h_{FR} (kg/m^2-s)
2.10E+06	6.89E+06	5.96	61.9	3.253E-02	939.5	2.030E+05	1.144E-01
3.03E+06	9.94E+06	5.99	62.5	4.708E-02	948.7	2.120E+05	1.396E-01
5.04E+06	16.54E+06	6.02	63.2	7.843E-02	957.5	2.213E+05	1.822E-01
6.63E+06	21.75E+06	6.04	62.6	1.023E-01	954.6	2.170E+05	2.074E-01
7.46E+06	24.48E+06	6.04	62.5	1.154E-01	953.6	2.167E+05	2.196E-01
8.34E+06	27.36+E-6	6.03	58.6	1.249E-01	918.1	1.791E+05	2.199E-01

C. Experimental Data Acquisition and Reduction

1. Data Acquisition and Reduction

Experimental data were obtained using the two-color, relative-intensity, global phosphor thermography method (Ref. 6) and reduced using the IHEAT (Imaging for Hypersonic Experimental Aerothermodynamic Testing) code (Ref. 7). In this method, a model is illuminated by ultraviolet light sources that induce temperature-dependent fluorescence of the phosphor coating. Fluorescent intensity images of a model are taken in the tunnel before and during a run using a three-color, charge-coupled device camera. The intensity data are converted to temperature using pretest calibrations of the data acquisition system and the temperature data are then processed to determine heat-transfer distributions.

Heat-transfer film coefficients are determined by assuming a step function in the film coefficient from the prerun temperature to the run temperature, which corresponds to a parabolic temperature-time history. The heating data are typically reported in terms of the ratio h/h_{FR} where the heat-transfer film coefficient, h, is defined in terms of enthalpy as $h = q/(H_{AW} - H_w) = q/(H_0 - H_w)$. In the calculation of the heat-transfer film coefficient, it is assumed that, for a blunt-body, the adiabatic wall enthalpy H_{AW} is equal to the free stream total enthalpy of the tunnel, H_0. This heat transfer coefficient definition provides a theoretically near-constant value over the course of a run since the decrease in time of the heat transfer rate in the numerator as the model surface becomes hotter is balanced by the decrease of the enthalpy-difference term in the denominator.

2. Data Mapping and Presentation

The two-dimensional (2-D) image data output from IHEAT for each run were transformed to account for optical perspective effects and mapped to a three-dimensional (3-D) CAD surface of the wind tunnel model. To accomplish this mapping, perspective, translational, and rotational transformations were first performed on the 3-D CAD surface until its 2-D projection matched that of the 2-D image data. The image data were then assigned transformed (x, y, z) coordinates based on interpolation between the image and surface geometry. Finally, the transformation was inverted to obtain an orthographic, 3-D heating distribution map of the experimental data.

An additional data manipulation was performed to extract the streamline-based heating distributions from the mapped wind tunnel data set. These streamline-based data sets are used in boundary-layer transition analyses and for comparisons of Reynolds number and hexcomb pattern effects. For each run, streamlines were defined based on the boundary-layer edge velocity vectors from the computed flow fields (to be discussed in the next section). Thirty-six streamline termini were established at locations spaced in 10 deg. increments around the circumference of the geometry and the streamlines were then traced backward from each terminus toward the flow field stagnation point. Each streamline is identified by the angular location, ϕ, of its terminus.

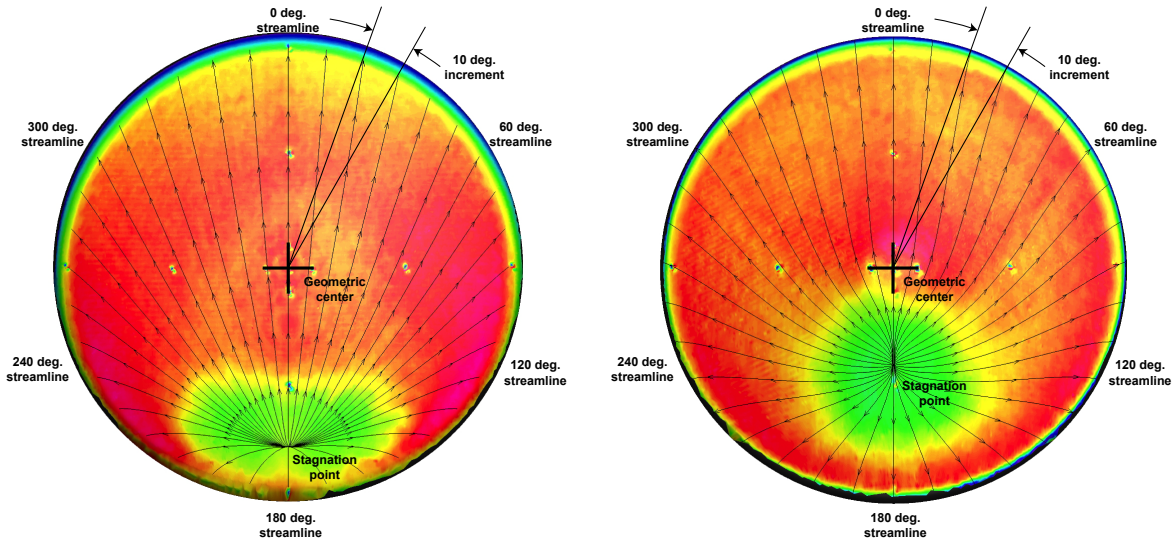
The resulting streamlines are shown in Figure 7a) for the spherical-cap geometry and in Figure 7b) for the sphere-cone geometry. The geometric definition (x, y, z) of each streamline was interpolated onto the 3-D mapped images and then data were extracted along each streamline in terms of h/h_{FR} vs. s/R, where s/R is the normalized streamline distance from the stagnation point. Additionally, the predicted flow field quantities (boundary-layer height, momentum-thickness Reynold number, etc.) were also extracted along these streamlines and combined with the experimental data set to enable transition onset analyses.

One complication needs to be noted with respect to extraction of data along streamlines. The extraction algorithm tended to fail near the stagnation point where the velocity vectors approach zero; essentially the physical location became indeterminate, resulting in unreliable path-lengths through the stagnation region. This problem was resolved by stopping the reverse tracing of the streamlines from the outer edge of the model toward that stagnation point at the location where the edge Mach number, M_e, dropped below 0.025. The "true" streamline length value, s_0 was determined from an estimate of the physical length from the M_e cutoff to the stagnation region as a function of the streamline terminus angular location ϕ and the approximate radius of the stagnation region, r_{stag}:

$$\boldsymbol{s_0 = s + \Delta s} \tag{1}$$

$$\boldsymbol{\Delta s = cos(2\phi) \times r_{stag}/3 + r_{stag}} \text{ , where } \boldsymbol{r_{stag}} \cong 0.003 \text{ m.} \tag{2}$$

In the body of this report, plotted data will be shown in terms of s/R, as that is the quantity in which the data were extracted along streamlines. However, the estimated actual distance, s_0/R, can be obtained using Eqs. 1-2.



a) Spherical-cap geometry **b) Sphere-cone geometry**

Figure 7. Streamlines for data extraction.

3. Experimental Uncertainty

The experimental uncertainty for convective heat transfer measurements on a smooth, blunt body geometry model in the 20-Inch Mach 6 Air Tunnel is quantified as a function of net uncertainties resulting from: the data acquisition method (±10%); flow quality and test-condition repeatability (±5%); and the accuracy of the 3D mapping process (±10%), which results in an overall root-sum-squared value of ±15%. Experience with this technique indicates that these values are usually conservative and as will be shown later, the predicted and measured heating distributions were in close agreement (generally less than ±5%) for laminar, smooth-wall cases. It is assumed that the hexcomb patterns introduced additional uncertainties for two reasons. First, the hexcomb cell walls were extremely thin, and the one-dimensional heat conduction assumption does not apply to them. Second, the hexcombs produced very detailed heating patterns, which in some cases, were smaller than the resolution of the camera system. Thus, a measurement in such areas is, in effect, a spatial average rather than a point measurement. Quantification of such errors on a macro-scale is not possible because of the localized and position/pattern dependency of hexcomb features, but is probably on the order of ±10-20%. Taken together with the smooth-wall uncertainty, the uncertainty in hexcomb heating is estimated to be in the ±18-25% range.

An additional factor that influences the quality of phosphor thermography data quality is the local surface inclination at a given point on the model with respect to both the camera and the illumination source. Phosphor thermography provides the best result when the surface to be imaged is normal to the camera, which reduces perspective distortion and image smearing, and when the surface is well illuminated by the ultraviolet lights, which induces the best temperature response of the phosphor coating. Because of the three-dimensional nature of a wind tunnel model, its entire surface cannot be optimally imaged, or in some cases cannot even be viewed. For blunt bodies such as those in this test, the windward centerline region of the model – the 'bottom' of the model with respect to the view orientation - is the area where the data quality was most affected. This situation is illustrated for a simple hemispherical geometry in Figure 8. Because of this limitation, windward centerline region data are only regarded as qualitative, not quantitative. Although image data from this region will be shown, quantitative plotted data and transition location data will not be provided for the streamlines originating from the 160 deg. through 200 deg. termini.

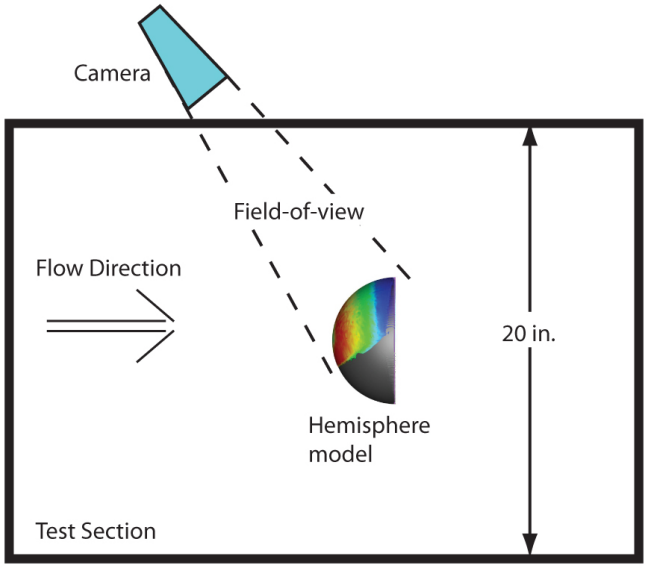


Figure 8. Illustration of camera field-of-view for hemisphere model in 20-Inch Mach 6 Air Tunnel.

D. Computational Tools and Methods

Flow field solutions were generated using the LAURA (Langley Aerothermodynamic Upwind Relaxation Algorithm) code. LAURA (Refs. 8-9) is a three-dimensional, structured-grid, finite-volume solver that includes perfect-gas and nonequilibrium chemistry options, a variety of turbulence models, and ablation and radiative transport capabilities. LAURA solutions were used for comparisons of predicted heating levels with the measured data and to define the streamlines along which to extract the mapped experimental data, as described above.

Solutions were computed on multiblock grids of each geometry with a smooth (no hexcombs) outer mold line. Grid adaption was performed to align the grid outer boundary with the bow shock and to cluster cells near the surface to produce wall cell Reynolds numbers on the order of 1 to 10. Free stream conditions were set to the nominal wind tunnel conditions for each run as given in Table 3. For these wind tunnel conditions, the perfect-gas air option was used. Both laminar and turbulent solutions were generated. Turbulent cases were computed using the Cebeci-Smith algebraic model with fully-turbulent flow over the entire geometry.

For the wall temperature boundary condition, a change in the normal practice for wind tunnel simulations of setting this value to a "cold-wall" ambient temperature (because of the usually small variation in heat-transfer coefficient with temperature) was employed. Literature on roughness effects indicates a dependence of transition onset location on the ratio of boundary-layer edge temperature to wall temperature T_e/T_w. To approximately account for this effect (which was expected to be small for these test conditions), the computations were performed using a uniform "hot-wall" wall temperature set to the average of the measured surface temperature on the model. These values varied between 327 K to 411 K, depending on roughness height and test condition.

IV. Experimental Results

A. Reynolds Number Effects on Heating and Transition

The effects of Reynolds number on the heating levels and boundary-layer transition onset locations are illustrated for the baseline smooth surface spherical-cap model in Figure 9 - Figure 10 and for the baseline smooth sphere-cone model in Figure 11 - Figure 12. Two figures are provided for each model: line plots of h/h_{FR} vs. s/R are shown in the first figure and global heating images are shown in the second. For brevity, all of the streamlines are not shown in these figures; instead, streamlines are shown at 30 deg. increments from 0 deg. to 150 deg. As noted earlier, the data for streamlines between 160 deg. and 200 deg. is considered to be qualitative, not quantitative. Data for streamlines from 210 deg. to 360 deg. are nominally symmetric with the data from 0 deg. to 150 deg., although in practice, model surface irregularities can cause asymmetric behavior. Such local asymmetries can be observed in the images that accompany the line plots. In general, the flow remained laminar on both smooth model geometries for the majority of test conditions. However, small transitional/turbulent wedges were produced on the sphere-cone model at the higher Reynolds numbers.

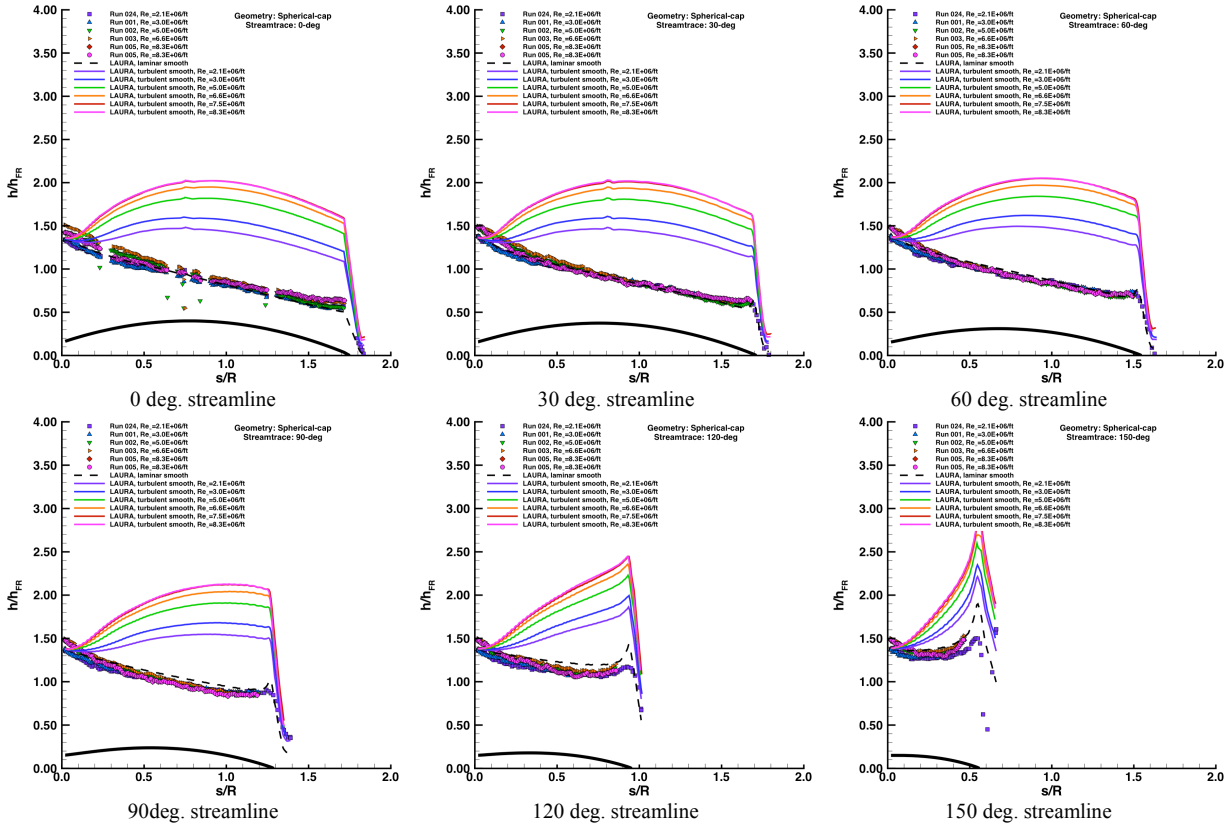
A sample set of figures for the hexcomb pattern roughness model (3700-0050 configuration) is shown in Figure 13 - Figure 14 for the spherical cap and in Figure 15 - Figure 16 for the sphere-cone. For brevity, the results from the other configurations are omitted, but they can be found in Ref. 1. As expected, the hexcomb pattern roughness produced earlier boundary-layer transition than was observed on the smooth model. Additionally, the heating levels downstream of transition were higher than those from the smooth-wall turbulent heating predictions.

In these line-plots, the LAURA predictions for smooth-wall, laminar and turbulent heating levels are also shown. Because the heat-transfer film coefficient ratio, h/h_{FR}, remains nearly constant with Reynolds number, only the lowest Reynolds number laminar prediction is included for each model. However, since this invariance does not hold for turbulent flow, turbulent predictions are shown for all Reynolds numbers. As noted previously, turbulent cases were treated as fully-turbulent flow over the entire geometry. These turbulent cases are shown as limiting bounds, since the actual transition occurred at different locations for each test condition / model geometry. Agreement to within less than the experimental uncertainty between the laminar predictions and the laminar data was observed for all cases except at the transitional/turbulent wedges for the higher Reynolds number sphere-cone model cases.

B. Configuration Effects on Heating and Transition

The effects of the hexcomb parameters on heating levels and boundary-layer transition are shown for an example case in Figure 17 - Figure 18 for the spherical-cap geometry and in Figure 19 - Figure 20 for the sphere-cone geometry. These examples are for the $Re_\infty = 5.0\times10^6$/ft condition. Results for the other Reynolds numbers can be found in Ref. 1. As expected, increasing the hexcomb depth caused transition to move upstream and caused the turbulent heating augmentation to increase. Additionally, the turbulent heating augmentation levels were slightly different for the coarse pattern spacing models (1200-xxxx) and the fine pattern spacing models (3700-xxxx) at some conditions. However, no clear trend with pattern spacing was identified, nor were there significant differences observed in the transition onset locations.

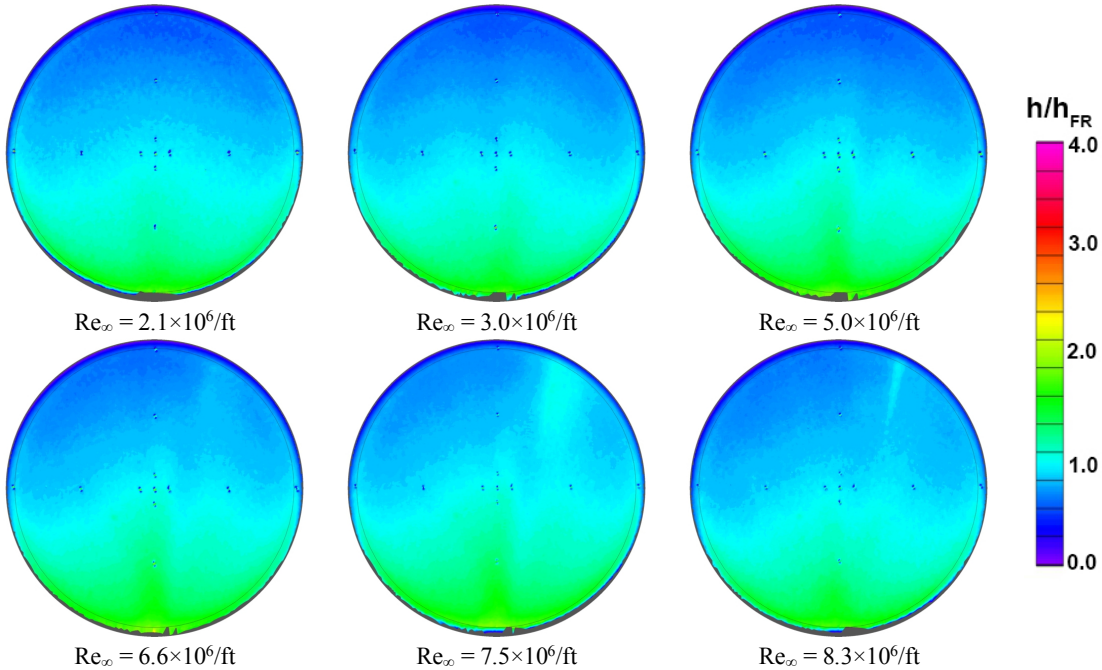
The lack of clear effects from pattern spacing variations is likely due to the relatively large aspect ratio of the hexcombs, with values ranging from $d/h = 6$ to 52. As defined by Refs. 10 - 11 and illustrated in Figure 21, all but the 3700-0050 and 3700-0100 hexcomb patterns fall into the "closed cavity" flow regime, in which the spacing between cavity walls is large enough for the flow to "close-down" to the bottom of the cavity, rather than skipping over and forming a recirculation bubble. For such closed cavity flows, the cavity distance is great enough that the cavity walls are effectively isolated from each other.



0 deg. streamline 30 deg. streamline 60 deg. streamline

90deg. streamline 120 deg. streamline 150 deg. streamline

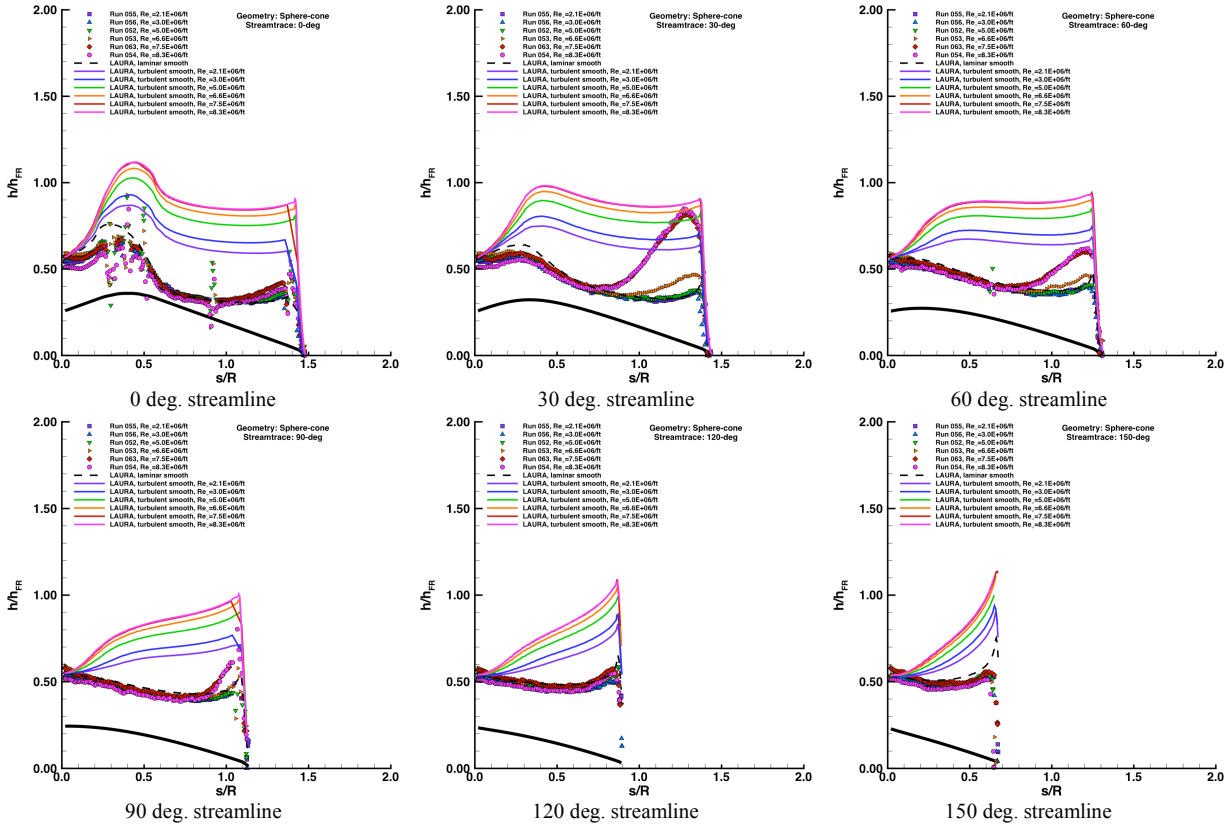
Figure 9. Reynolds Number effects, spherical-cap smooth model plots.



$Re_\infty = 2.1\times10^6$/ft $Re_\infty = 3.0\times10^6$/ft $Re_\infty = 5.0\times10^6$/ft

$Re_\infty = 6.6\times10^6$/ft $Re_\infty = 7.5\times10^6$/ft $Re_\infty = 8.3\times10^6$/ft

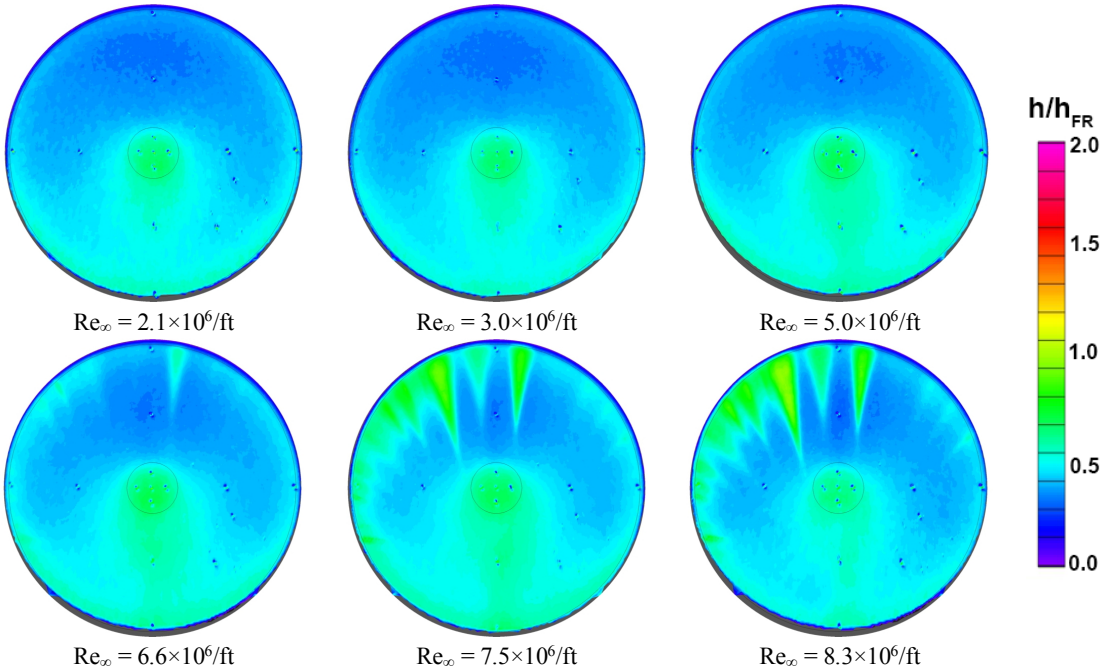
Figure 10. Reynolds Number effects, spherical-cap smooth model images.



0 deg. streamline | 30 deg. streamline | 60 deg. streamline

90 deg. streamline | 120 deg. streamline | 150 deg. streamline

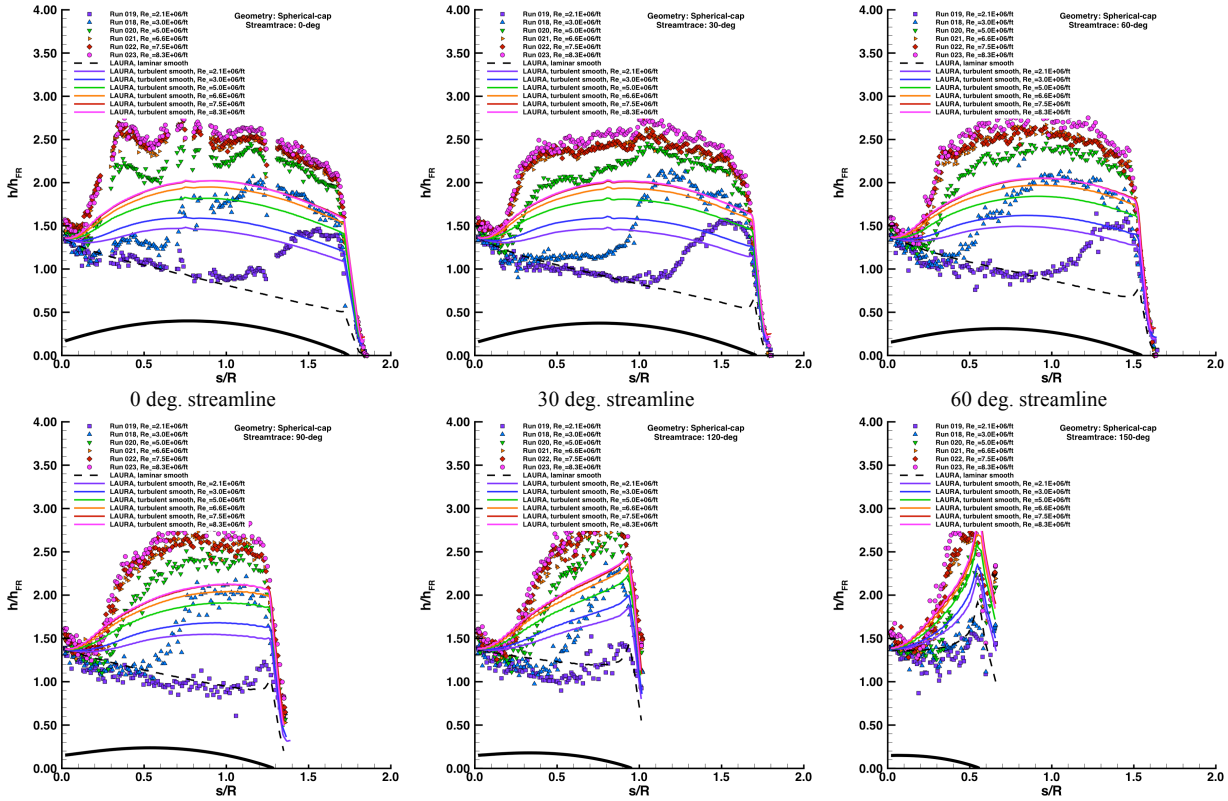
Figure 11. Reynolds Number effects, sphere-cone smooth model plots.



$Re_\infty = 2.1\times10^6$/ft | $Re_\infty = 3.0\times10^6$/ft | $Re_\infty = 5.0\times10^6$/ft

$Re_\infty = 6.6\times10^6$/ft | $Re_\infty = 7.5\times10^6$/ft | $Re_\infty = 8.3\times10^6$/ft

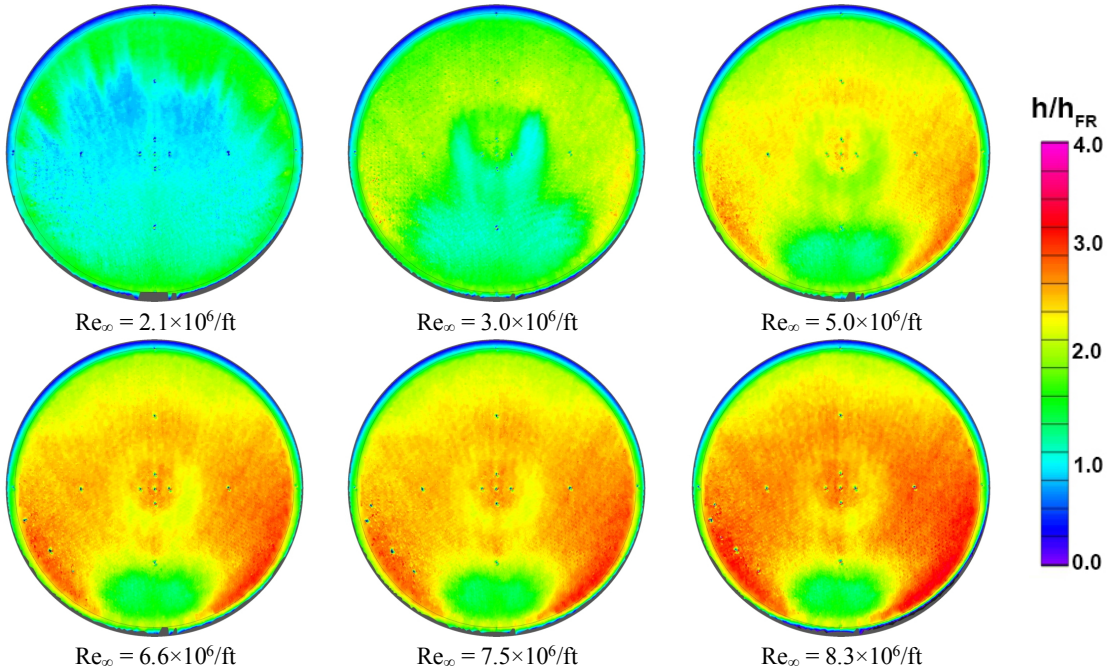
Figure 12. Reynolds Number effects, sphere-cone smooth model images.



0 deg. streamline | 30 deg. streamline | 60 deg. streamline

90 deg. streamline | 120 deg. streamline | 150 deg. streamline

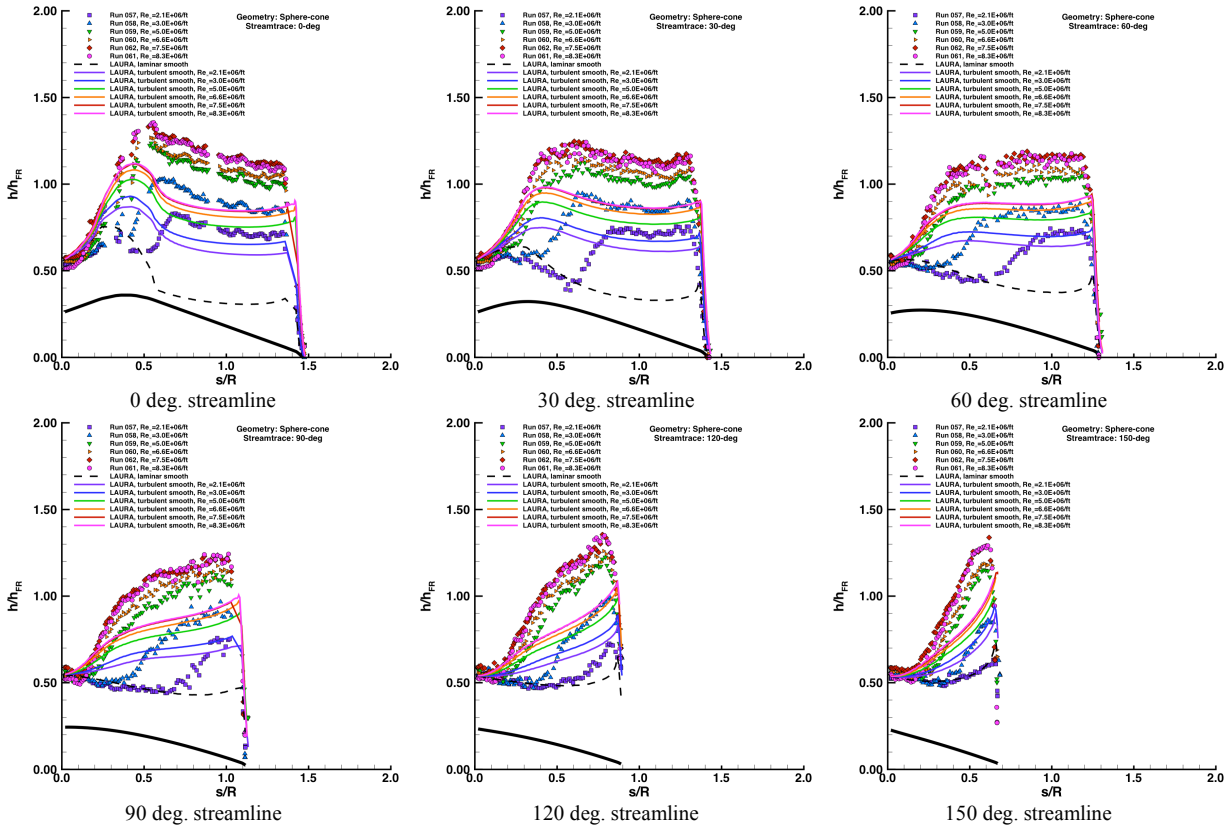
Figure 13. Reynolds Number effects, spherical-cap 3700-0050 model plots.



$Re_\infty = 2.1\times10^6$/ft | $Re_\infty = 3.0\times10^6$/ft | $Re_\infty = 5.0\times10^6$/ft

$Re_\infty = 6.6\times10^6$/ft | $Re_\infty = 7.5\times10^6$/ft | $Re_\infty = 8.3\times10^6$/ft

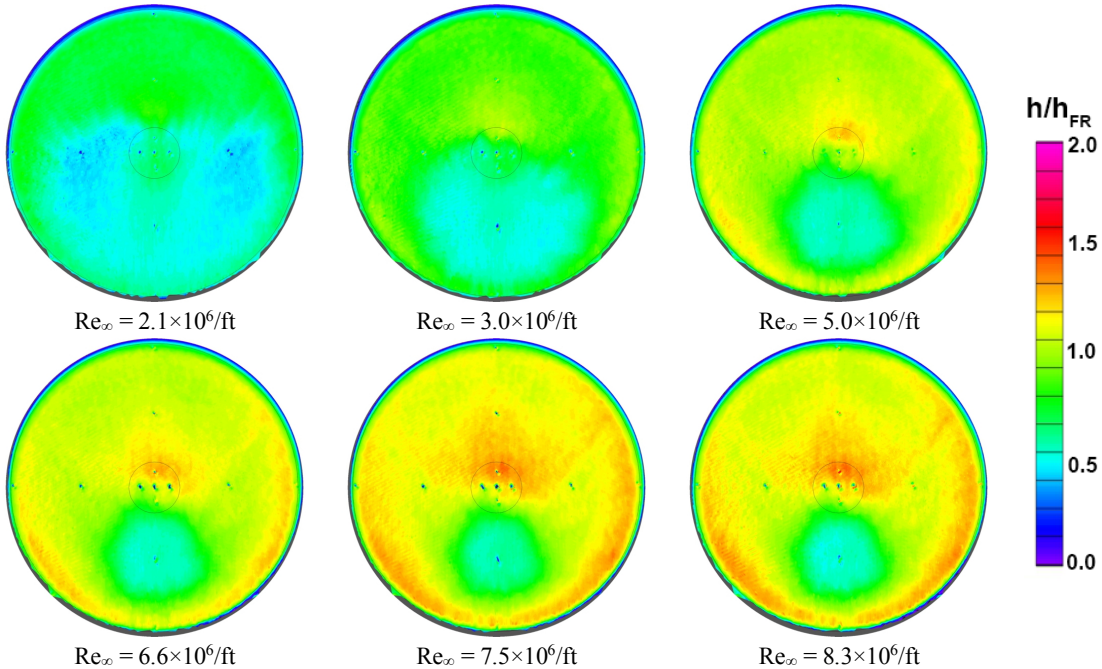
Figure 14. Reynolds Number effects, spherical-cap 3700-0050 model images.



0 deg. streamline | 30 deg. streamline | 60 deg. streamline

90 deg. streamline | 120 deg. streamline | 150 deg. streamline

Figure 15. Reynolds Number effects, sphere-cone 3700-0050 model plots.



$Re_\infty = 2.1\times10^6$/ft | $Re_\infty = 3.0\times10^6$/ft | $Re_\infty = 5.0\times10^6$/ft

$Re_\infty = 6.6\times10^6$/ft | $Re_\infty = 7.5\times10^6$/ft | $Re_\infty = 8.3\times10^6$/ft

Figure 16. Reynolds Number effects, sphere-cone 3700-0050 model images.

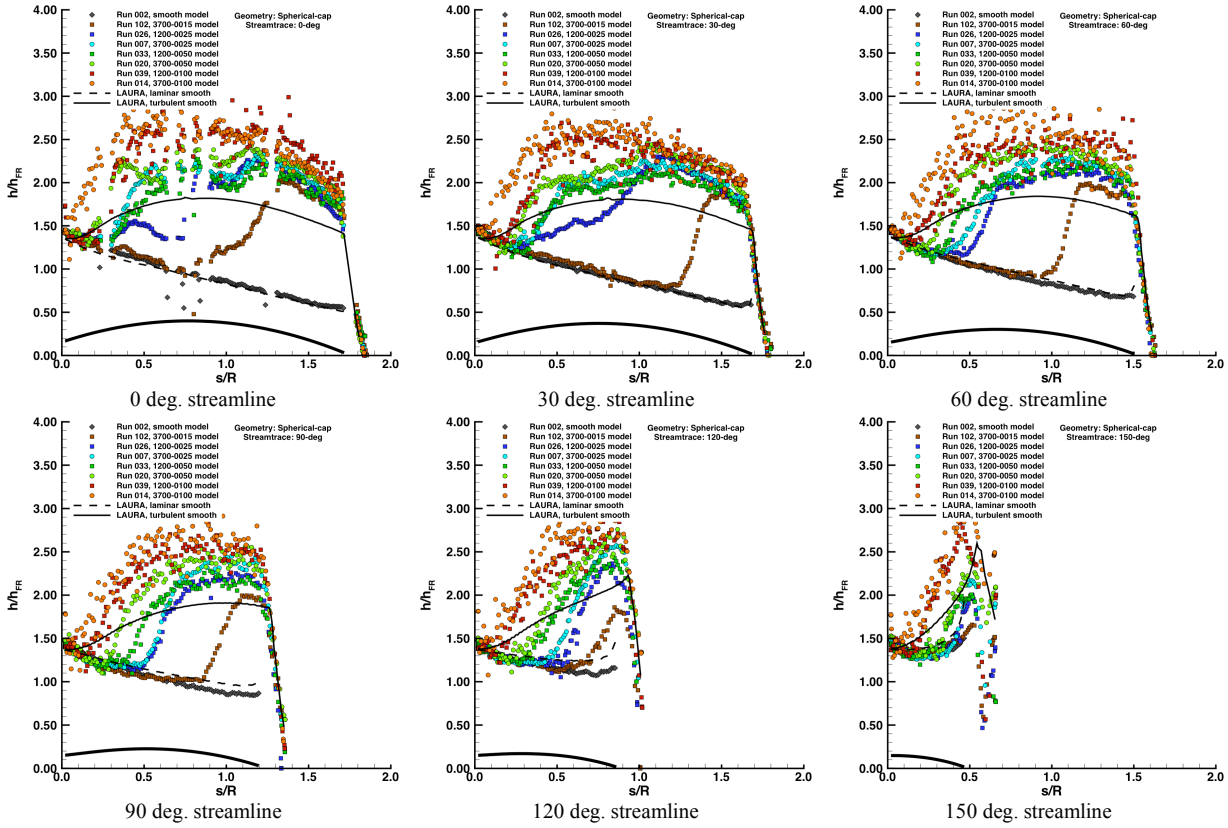


Figure 17. Hexcomb pattern effects, spherical-cap geometry, $Re_\infty = 5.0\times10^6$/ft plots.

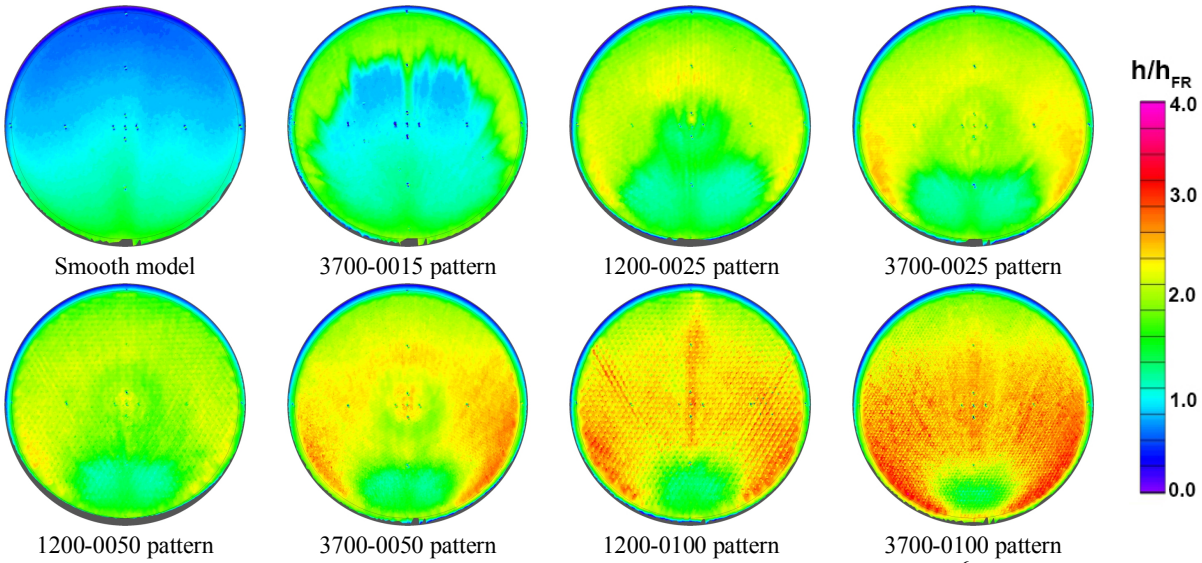


Figure 18. Hexcomb pattern effects, spherical-cap geometry, $Re_\infty = 5.0\times10^6$/ft images.

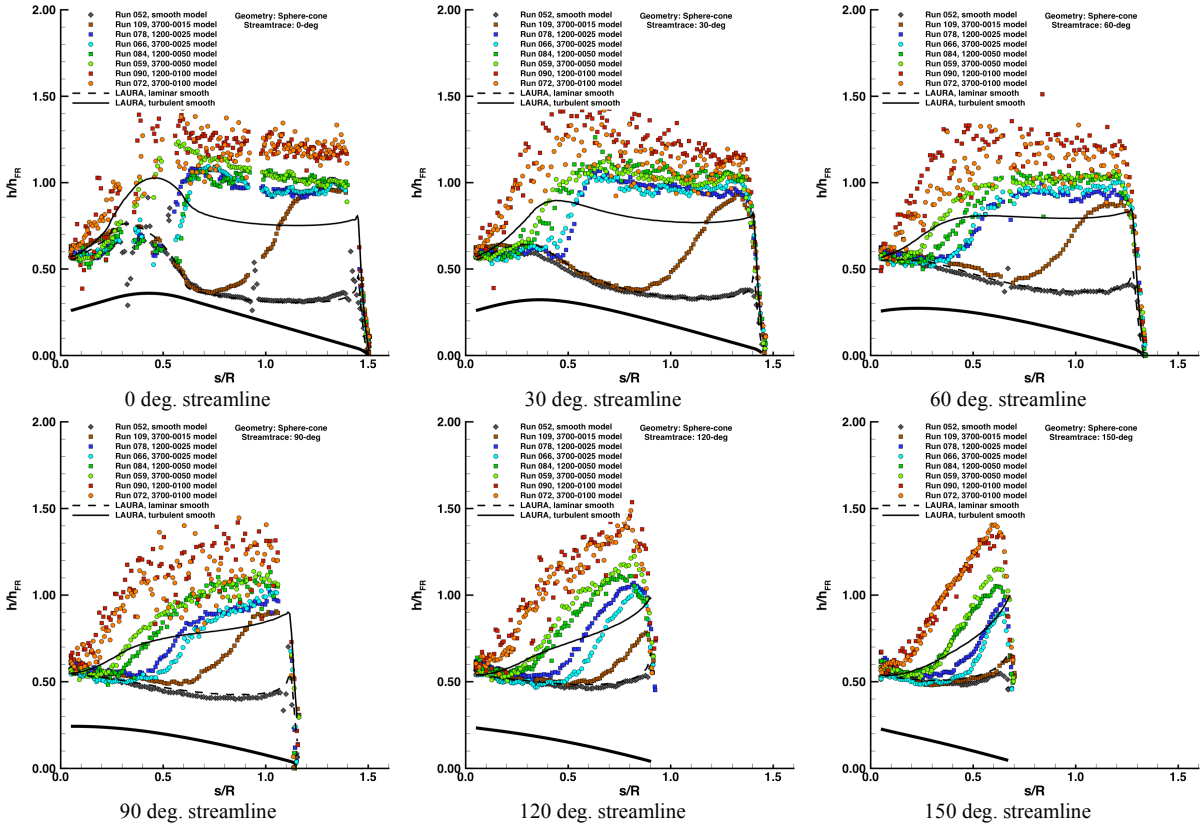


Figure 19. Hexcomb pattern effects, sphere-cone geometry, $Re_\infty = 5.0\times10^6$/ft plots.

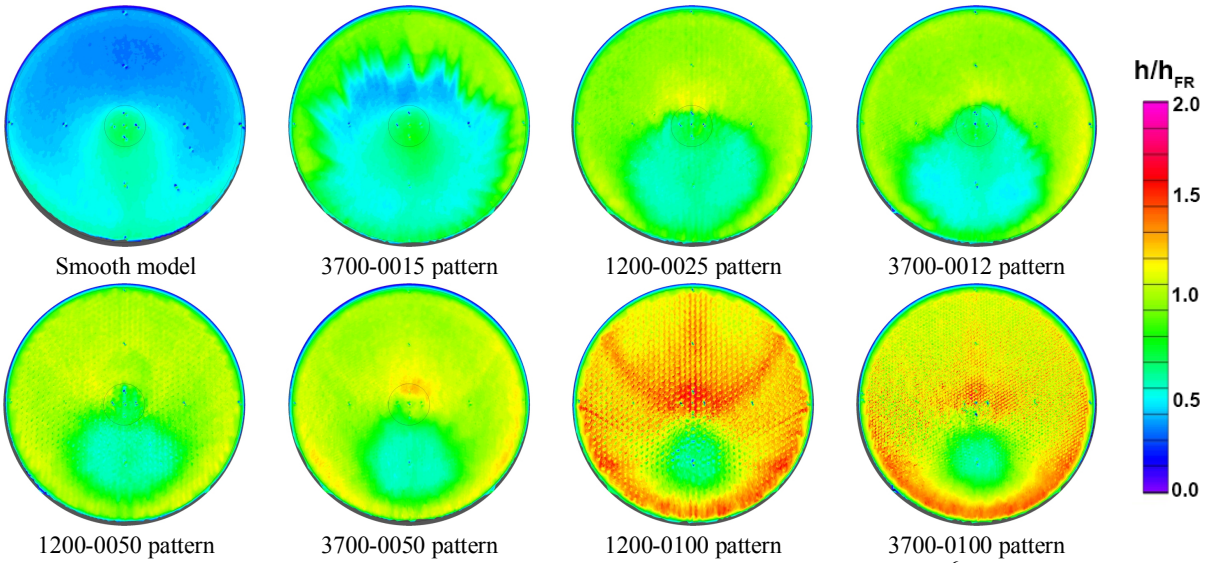


Figure 20. Hexcomb pattern effects, sphere-cone geometry, $Re_\infty = 5.0\times10^6$/ft images.

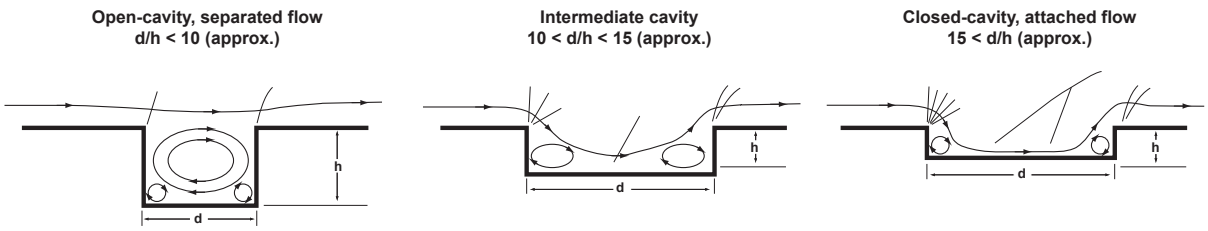


Figure 21. Illustration of open and closed cavity flow regimes.

C. Boundary Layer Transition Correlation

Boundary-layer transition onset locations were determined for all streamlines at each test condition through examination of the Reynolds number effects line plots of heating vs. streamline distance. Following the procedure detailed in Ref. 1, transition onset locations were identified through the tangent-slope-intercept method. This method provides a consistent "apparent" transition location that can be clearly determined through analysis of surface temperature or heat transfer data. However, this location is effectively slightly downstream of the point in the boundary-layer at which the small disturbances that produce transition actually begin.

In all, this test program provided 3024 potential measurements (36 streamlines *x* 6 Reynolds numbers *x* 7 hexcomb patterns *x* 2 geometries) of transition location over relevant three-dimensional entry vehicle geometries. After discounting the data from streamlines ϕ = 160 - 200 deg. due to the viewing angle difficulty, and also discounting those low Reynolds number / small hexcomb depth cases where the flow remained laminar and the high Reynolds number / large hexcomb depth where the flow was turbulent at the stagnation point, 1892 actual data points were generated. These transition onset data points are tabulated in Ref. 1.

In Ref. 12, a database of 451 transition onset locations on hemispherical nosetip geometries from flight, wind tunnel, and ballistics range tests was assembled and analyzed in order to correlate the effects of distributed, sandgrain type roughness on boundary-layer transition. The resulting correlation is given by the equation:

$$Y_{TR} = 165 \times (X_{TR})^{-0.5} \tag{3}$$

where the flow field parameter Y_{TR} is:

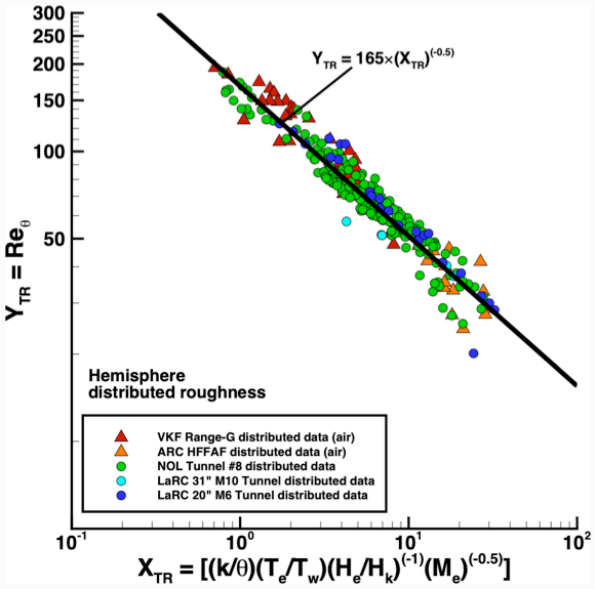
$$Y_{TR} = (Re_\theta)_{TR} \tag{4}$$

and the disturbance parameter X_{TR} is:

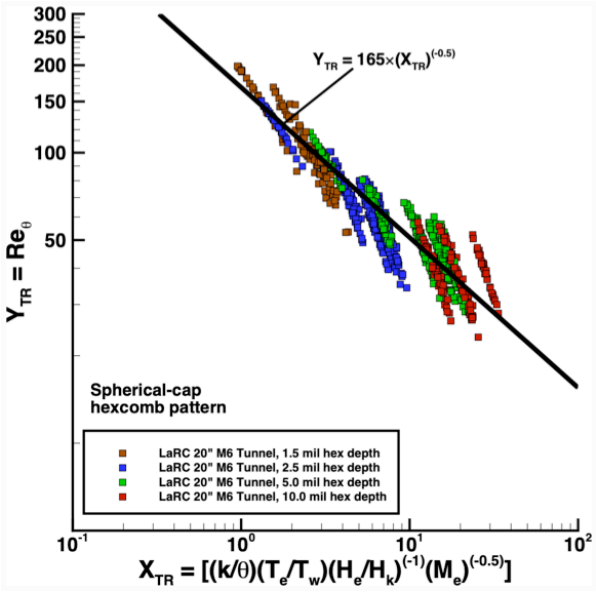
$$X_{TR} = \left[\left(\frac{k}{\theta}\frac{T_e}{T_w}\right)\left(\frac{H_e}{H_k}\right)^{-1}(M_e)^{-0.5}\right]_{TR} \tag{5}$$

In this correlation, the roughness height parameter *k* was taken to be the 50% peak-to-valley exceedance value k_{PV50}, as defined in Ref. 12. As shown in Figure 22-a), the formulation was found to be effective in correlating the wide range of database conditions.

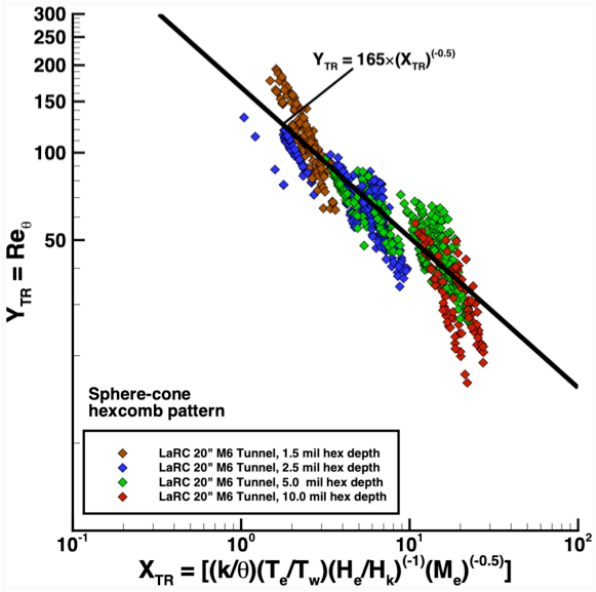
The sandgrain distributed roughness correlation was used as the starting point for analysis of the current hexcomb pattern roughness dataset with the roughness height for hexcombs set to the hexcomb depth, *h*. Unfortunately, as shown in Figure 22-b) and Figure 22-c), this correlation did not provide an adequate representation of the hexcomb data. Although the hexcomb pattern roughness data follow the same first-order trend as the sandgrain distributed roughness data, the regular "banding" of the data points clearly indicated a dependency that is not represented by this definition of the disturbance parameter.



a) Applied to hemisphere models with sandgrain roughness



b) Applied to spherical-cap models with hexcomb pattern roughness



c) Applied to sphere-cone models with hexcomb pattern roughness

Figure 22. Original sandgrain distributed roughness transition correlation.

There were two possible reasons considered for the failure of the distributed roughness correlation: 1) inherent differences in the transition mechanism of hemispherical distributed sandgrain roughness elements and hexcomb array roughness elements; and 2) differences in flow field behavior and boundary-layer parameters between axisymmetric hemispheres and the three-dimensional spherical-cap and spherical cone models.

Attempts were made to reconcile the sandgrain and hexcomb roughness effects through "shape-factors" multipliers of the roughness height that were defined in terms of the roughness element parameters (height, spacing, width, etc.). However, no shape-factor definition could be found that reconciled the two data sets.

Success in correlating both data sets was instead achieved through redefinition of the disturbance parameter to account for the three-dimensionality of the spherical-cap and sphere-cone flow fields with an additional term derived from the Pohlhausen parameter:

$$\beta_{POHL} = \left\{10^{[min(10,max(-10,\lambda_{POHL}))]/10}\right\}^{-1} \tag{6}$$

where the Pohlhausen parameter is defined as:

$$\lambda_{POHL} = \frac{dU_e}{ds}\frac{\delta^2}{\nu_e} \tag{7}$$

The complicated definition for this modified Pohlhausen parameter, β_{POHL}, is required to ensure that the value remains bounded and positive. The Pohlhausen parameter is a pressure-gradient term that can be positive or negative over the surface. The exponentiation of the term ensures that the value is positive, and the min/max limits ensure that the value does not cause computational under/over flow.

The exponents on the modified Pohlhausen parameter and the original components of the disturbance terms were parametrically varied to find a new best fit definition as:

$$X_{TR} = \left[\left(\frac{k}{\theta}\frac{T_e}{T_w}\right)^{0.45}\left(\frac{H_e}{H_k}\right)^{-1.8}(M_e)^{-0.6}(\beta_{POHL})^{-0.5}\right]_{TR} \tag{8}$$

where

$$k = \begin{cases} k_{PV50} & \text{sandgrain distributed} \\ h & \text{hexcomb pattern} \end{cases} \tag{9}$$

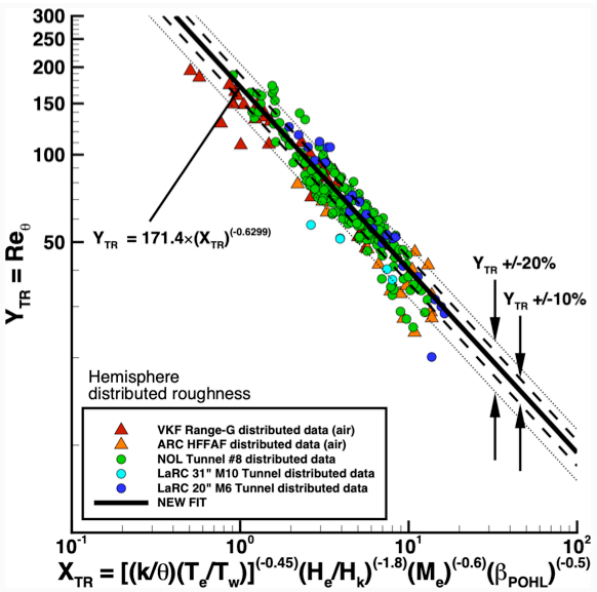
The new correlation equation for both distributed sandgrain and hexcomb pattern roughness is then given by:

$$Y_{TR} = 171.4 \times (X_{TR})^{-0.6299} \tag{10}$$

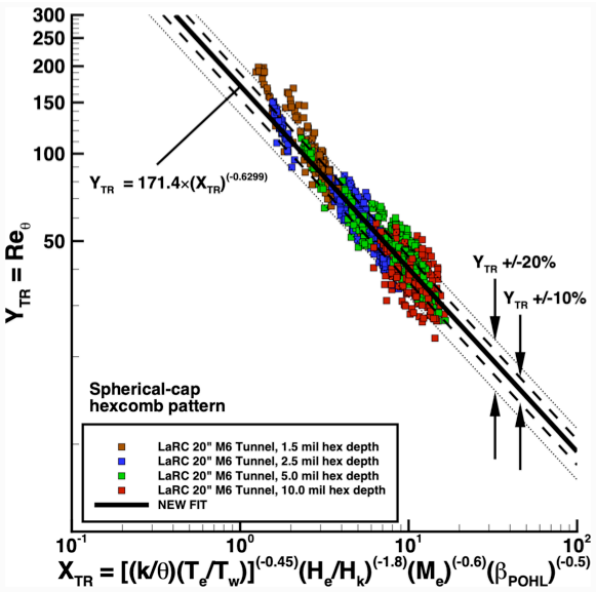
As shown in Figure 23-a) - Figure 23-c) this new correlation provides an excellent representation of both data sets. The majority of the transition data fall within ±20% of the correlation prediction. The only significant deviations from the correlation occur at the min/max limits of small roughness, low Reynolds number and large roughness, high Reynolds numbers parameters.

The application of this new sandgrain/hexcomb distributed roughness correlation to transition prediction is shown graphically in Figure 24 - Figure 25 for sample spherical-cap and sphere-cone cases. In these images, the computed flow field parameters were used to generate surface contour maps of $Re_{\theta,TR}/Re_{\theta}$, which is the ratio of the critical transition momentum thickness Reynolds number to the local value. Transition should then occur in the green contour band where this value is near to one. Overlaid on these maps are the data points representing the measured transition onset locations for each streamline (omitting the ϕ = 160 – 200 deg. streamlines). Almost all data points fall between the red and blue boundaries, which represent the ±20% margins on the correlation. In fact, almost all data points fall between the yellow and cyan bounds that represent ±10% margins on the correlation.

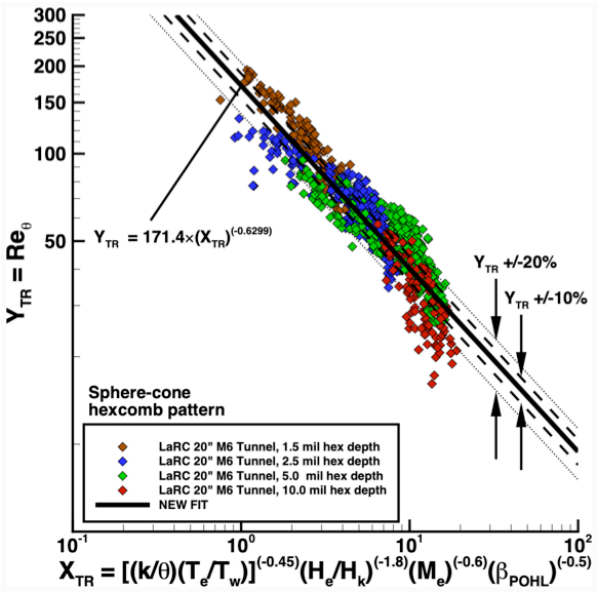
Although this correlation accurately represents the data, there remains the potential for updates to this formulation. The earlier sandgrain distributed roughness correlation for hemispherical models required modifications to incorporate the new hexcomb pattern roughness data for spherical-cap and sphere-cone models. Similarly, future databases may lead to updates to this correlation. Areas of interests for future research include: sandgrain distributed roughness on spherical-cap and sphere-cone geometries to supplement the existing hemisphere geometry database; high-enthalpy roughness transition data to address questions noted in Ref 12.; and also woven and block TPS step/gap roughness data.



a) Applied to hemisphere models with sandgrain roughness



b) Applied to spherical-cap models with hexcomb pattern roughness



c) Applied to sphere-cone models with hexcomb pattern roughness

Figure 23. New sandgrain distributed and hexcomb pattern distributed roughness transition correlation.

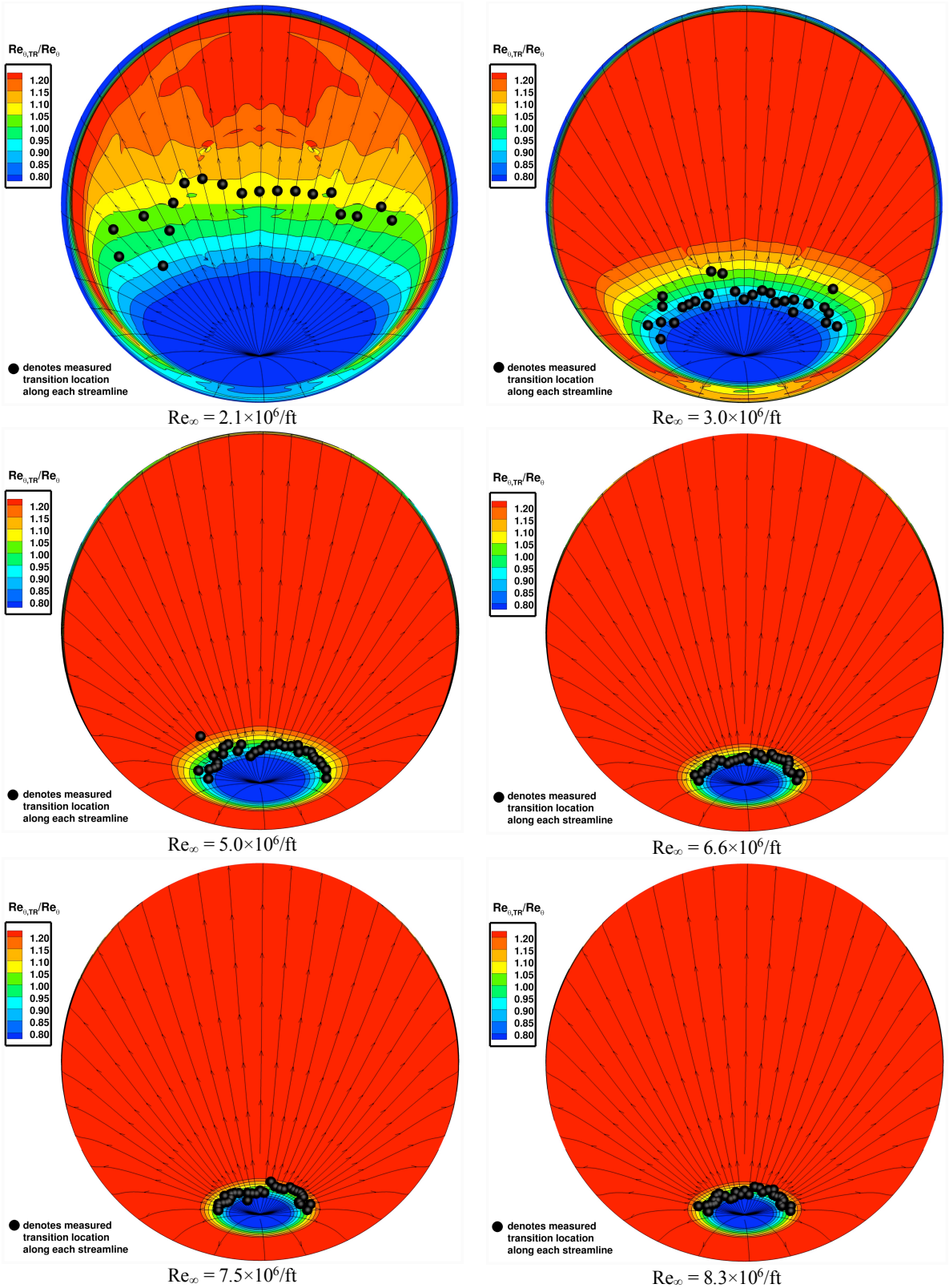


Figure 24. Predicted and measured transition onset locations, spherical-cap 3700-0050 model.

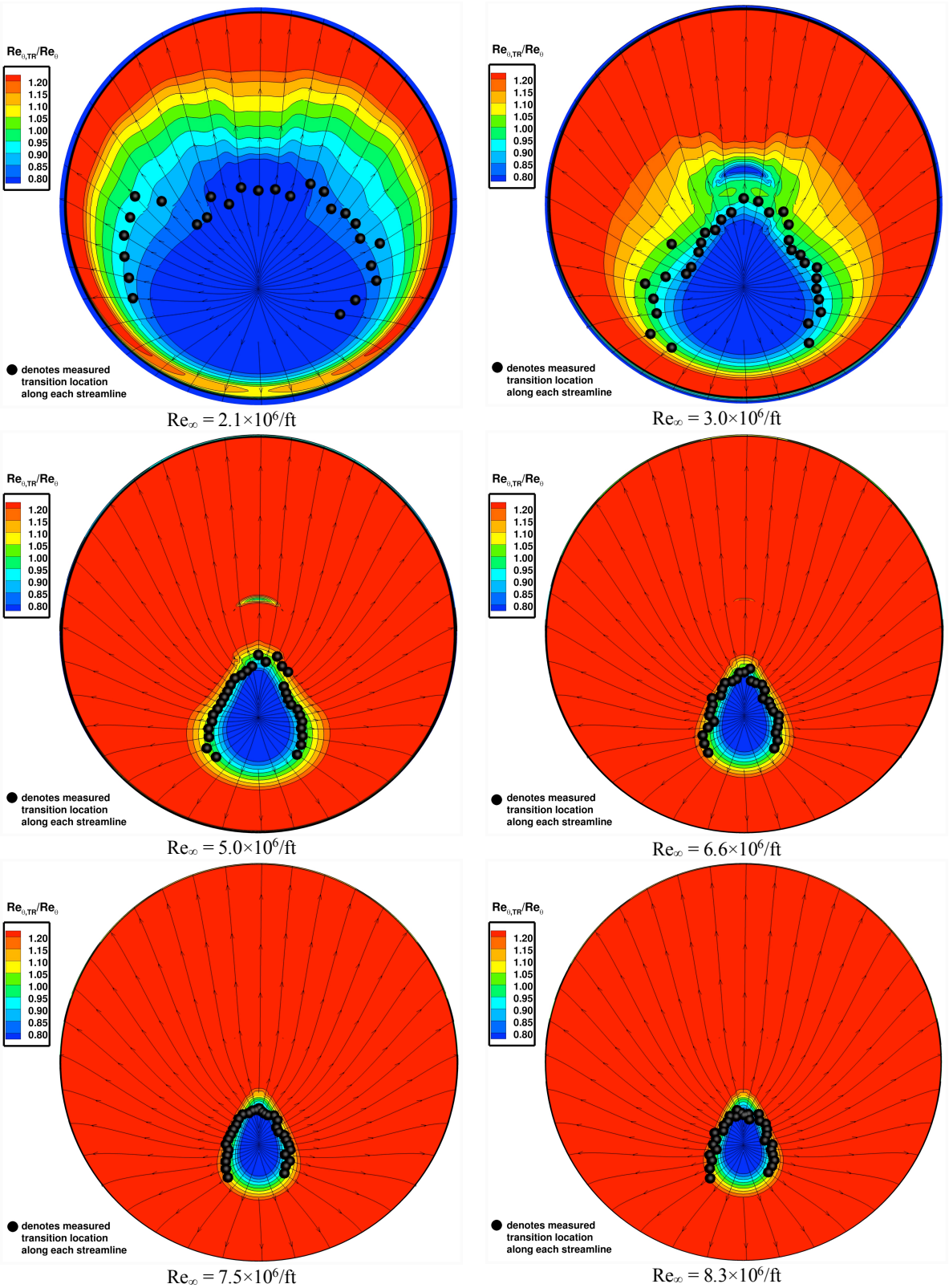


Figure 25. Predicted and measured transition onset locations, sphere-cone 3700-0050 model.

V. Summary and Conclusions

The effects of hexcomb pattern distributed surface roughness on boundary-layer transition and turbulent heating have been investigated through hypersonic wind tunnel testing of two representative entry vehicle geometries with roughness patterns simulating those of a heat shield with an ablated TPS. Convective heating data were obtained at Mach 6 over a range of roughness heights and free stream Reynolds numbers sufficient to produce laminar, transitional and turbulent flow. Boundary-layer transition onset locations were extracted along multiple surface streamlines for each model.

Laminar and turbulent smooth surface computational flow field simulations were performed for all test conditions for comparison with the heating data and to provide boundary-layer parameters for correlation of the transition data. The smooth surface laminar heating data and predictions were in good agreement for all conditions. The measured turbulent heating augmentation above smooth-wall predictions grew larger with increasing hexcomb depth.

A boundary-layer transition correlation developed from an earlier sandgrain distributed roughness data set on hemispherical geometries was evaluated for use with the hexcomb pattern data. This formulation was found to be insufficient for correlation of the current data set. A new combined sandgrain and hexcomb pattern distributed roughness correlation was developed from the two data sets that resulted in excellent correlation of all data. However, the potential remains for updates to this correlation as additional roughness data are acquired.

VI. Acknowledgements

This work was supported by the NASA Entry Systems Modeling Project within the Game Changing Development Program of the Space Technology Mission Directorate.

VII. References

1. Hollis, B. R., "Experimental Investigation of Hexcomb-Pattern Roughness Effects on Transition Onset and Turbulent Heating Augmentation at Mach 6," NASA-TM-2019-220424, November, 2019.
2. Loomis, M. P., Prabhu, D. K., Gorbunov, S., Olson, M., and Vander Kam, J., "Results and Analysis of Large Scale Article Testing in the Ames 60 MW Interaction Heating Arc Jet Facility," AIAA Paper 2010-0445, AIAA Aerospace Sciences Meeting, January 2010, Orlando, FL.
3. Berger, K., Rufer, S., Hollingsworth, K. and Wright, S., "NASA Langley Aerothermodynamic Laboratory: Hypersonic Testing Capabilities," AIAA Paper 2015-1337, 53rd AIAA Aerospace Sciences Meeting, Kissimmee, FL, January 5-9, 2015.
4. Hollis, B. R., Berger, K. T., Berry, S. A., Brauckmann, G. J., et al, "Entry, Descent, and Landing Aerothermodynamics: NASA Langley Experimental Capabilities and Contributions," AIAA Paper 2014-1154, AIAA 52nd Aerospace Science Meeting, National Harbor, MD, January 13-17, 2014.
5. Fay, J. A., and Riddell, F. R., "Theory of Stagnation Point Heat Transfer in Dissociated Air," *Journal of Aeronautical Sciences*, Vol. 25, No. 2., February 1958, pp. 73-85.
6. Buck, G. M., "Surface Temperature/Heat Transfer Measurement Using a Quantitative Phosphor Thermography System," AIAA Paper 91-0064, 29th Aerospace Sciences Meeting, Reno, NV, January 7-10, 1991.
7. Merski, N. R., "Global Aeroheating Wind-Tunnel Measurements Using Improved Two-Color Phosphor Thermography Methods," *Journal of Spacecraft and Rockets*, Vol. 36, No. 2, March-April 1999, pp. 160-170.Hollis, B. R., "Blunt-Body Entry Vehicle Aerothermodynamics: Transition and Turbulent Heating," Journal of Spacecraft and Rockets, Vol. 49, No. 3, May-June 2012, pp. 435-449.
8. Gnoffo, P. A., "An Upwind-Biased, Point-Implicit Algorithm for Viscous, Compressible Perfect-Gas Flows," NASA TP-2953, February 1990.
9. Mazaheri, A., Gnoffo, P. A., Johnston, C. O., and Kleb, B., "LAURA User's Manual: 5.5-65135," NASA TM-2013-217800, February 2013.
10. Charwat, A. F., Roos, J. N., Dewy, C. F., and Hitz, J. A., "An Investigation of Separated Flow: Part 1, the Pressure Field," *Journal of the Aero/Space Sciences*, Vol. 28, No. 6, June 1961, pp. 457–470.
11. Charwat, A. F., Dewey, C. F., Roos, J. N., and Hitz, J. A., "An Investigation of Separated Flow: Part 2, Flow in the Cavity and Heat Transfer," *Journal of the Aero/Space Sciences*, Vol. 28, No. 7, July 1961, pp. 513–527.
12. Hollis, B. R., "Correlation of Recent and Historical Hemispherical Nose Tip Distributed Roughness Transition Data," *Journal of Spacecraft and Rockets*, Vol. 56, No. 3, May-June 2019, pp. 664-686.